OPEN ACCESS
Journal of Multidisciplinary Applied Natural Science Vol. xx No. xx (xxxx) https://doi.org/10.47352/jmans.2774-3047.354
Check for updates
Research Article

Assessing the Magnetic Shielding Effectiveness of Low Carbon Steel, Permalloy, and Mu-metal on Small Satellite Reaction Wheel Assemblies using Finite Element Analysis

Hogan Eighfansyah Susilo*, Poki Agung Budiantoro, Ery Fitrianingsih, Hasan Mayditia, Eriko Nasemudin Nasser, Adi Farmasiantoro, Ahmad Fauzi, Widodo Slamet, Andi Mukhtar Tahir, and Nindhita Pratiwi

Received : October 23, 2025	Revised : December 28, 2025	Accepted : January 2, 2026	Online : January 23, 2026

Abstract
Magnetic cleanliness is essential for small satellites carrying sensitive payloads such as magnetometers and particle detectors. Reaction wheel assemblies (RWAs) represent a primary source of stray magnetic fields, requiring effective shielding under strict mass and volume constraints. This study uses three-dimensional finite element analysis (FEM) in ANSYS Maxwell to evaluate the shielding effectiveness (SE) of high-permeability alloys (Mu-metal and Permalloy 80) and low-carbon steels (AISI 1008/1010) at thicknesses of 1–3 mm, with aluminum 6061-T6 as a non-magnetic baseline, within a cylindrical RWA enclosure geometry. Results reveal a critical design trade-off: High-permeability alloys provide superior attenuation (>65 dB at 100 mm; residual field <150 nT) and high mass efficiency (>700 dB/kg) but saturate at low flux density (0.8 T) and are costly. Low-carbon steels offer moderate SE (34–40 dB) with far higher saturation tolerance (2.2 T), structural robustness, and lower cost. Thickness scaling shows diminishing returns beyond 2 mm for high-permeability materials, whereas steels improve more linearly. Rather than proposing a new shielding concept, this study applies an integrated FEM-based evaluation approach for small satellite platforms to consistently assess shielding effectiveness, nonlinear saturation behavior, thickness scaling, and mass efficiency of candidate materials within a reaction-wheel-representative geometry under identical boundary conditions.

Keywords: finite element analysis, magnetic cleanliness, magnetic shielding, reaction wheel assembly, shielding effectiveness, small satellites

1. INTRODUCTION

Magnetic cleanliness is a critical design requirement for spacecraft carrying magnetically sensitive payloads, including fluxgate magnetometers, charged-particle detectors, and precision attitude sensors. To ensure measurement accuracy and long-term stability, space agencies impose stringent limits on allowable magnetic emissions. International standards such as ECSS-E-ST-20-07C and NASA's General Environmental Verification Standard (GEVS) define verification procedures and permissible static and time-varying magnetic field levels, emphasizing system-level cleanliness planning, component placement, and mitigation strategies throughout the mission lifecycle [1]-[3].

Achieving compliance with these requirements is particularly challenging for small satellite platforms, where compact integration, limited subsystem separation, and strict mass and volume constraints dominate the design space. Most small satellites operating in low Earth orbit (LEO) employ attitude control architectures based on reaction wheels combined with magnetorquers, as demonstrated by missions such as LAPAN-TUBSAT [4], LAPAN-A2 [5], and LAPAN-A3 [6]. In LEO, spacecraft are subject to multiple disturbance torques, including aerodynamic drag, gravity-gradient effects, and geomagnetic interactions [7]-[9]. Among these, torques arising from the spacecraft's residual magnetic dipole moment are often significant, particularly for missions hosting magnetically sensitive payloads [10].

Residual magnetic dipoles originate from several onboard subsystems, including electric motors, batteries, power distribution cabling, and magnetic actuators. Within the attitude determination and control subsystem (ADCS), reaction wheel assemblies (RWAs) are widely recognized as dominant and persistent sources of onboard magnetic contamination. RWAs generate both static

Please cite this article as: H. E. Susilo, P. A. Budiantoro, E. Fitrianingsih, H. Mayditia, E. N. Nasser, A. Farmasiantoro, A. Fauzi, W. Slamet, A. M. Tahir, and N. Pratiwi. (2026). "Assessing the Magnetic Shielding Effectiveness of Low Carbon Steel, Permalloy, and Mu-metal on Small Satellite Reaction Wheel Assemblies using Finite Element Analysis". *Journal of Multidisciplinary Applied Natural Science*. https://doi.org/10.47352/jmans.2774-3047.354

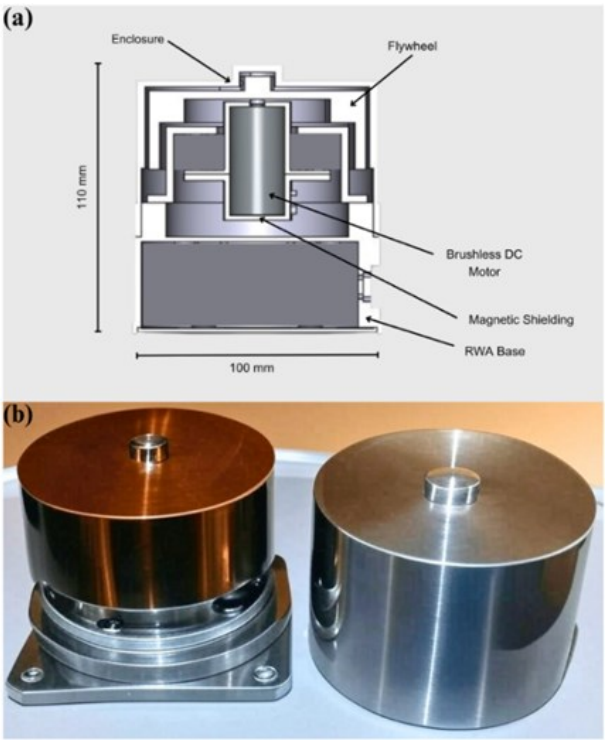

Figure 1. (a) The 3D CAD model of the RWA assembled with the proposed magnetic shielding enclosure, and (b) a comparative RWA design for small satellites under 200 kg.

and time-varying magnetic fields associated with permanent-magnet rotors, stator currents, and drive electronics, which can couple into sensitive payload regions when separation distances are limited to only a few tens of centimeters.

Mitigation strategies for spacecraft magnetic emissions generally include passive approaches, such as optimized component placement and layout [11]-[13], as well as active cancellation methods employing compensation coils [14][15]. While active approaches can be effective, they are often impractical for small satellites due to power limitations, increased system complexity, and tight volume constraints. Furthermore, RWA magnetic emissions vary dynamically with wheel speed and operational mode, complicating real-time compensation and reducing robustness under flight conditions. Consequently, passive magnetic shielding remains the most practical mitigation strategy for small satellite platforms.

Reaction wheel magnetic emissions comprise both static and time-varying components. The static component is primarily generated by the permanent -magnet rotor, while time-varying fields arise from stator currents, commutation effects, and drive electronics. Prior experimental and numerical studies have demonstrated that, under nominal operating conditions, rotor-induced static fields dominate the near-field magnetic environment of compact RWAs and govern saturation-limited shielding behavior [15]-[19]. Accordingly, this study restricts the analysis to the magnetostatic field generated by the permanent-magnet rotor. This modeling choice captures a conservative worst-case condition for passive magnetic shielding, in which high-permeability materials are most susceptible to nonlinear saturation, while preserving the relative ranking of candidate materials and thickness-dependent attenuation trends.

Passive magnetic shielding mitigates stray fields by redirecting magnetic flux into materials with high magnetic permeability. High-permeability alloys such as Mu-metal and Fe–Ni permalloy are widely used for attenuating static and low-frequency magnetic fields, with reported attenuation levels exceeding 50–60 dB in controlled configurations [20][21]. However, these materials are limited by low saturation flux density, relatively high density, mechanical fragility, and elevated cost, constraining their applicability in mass- and volume-limited spacecraft [22]. In contrast, low-carbon steels such as AISI 1008 and AISI 1010

exhibit moderate permeability but significantly higher saturation flux density, improved mechanical robustness, and lower cost, enabling structurally integrated or mass-efficient shielding solutions [23] [24].

Flight heritage highlights the practical implications of these trade-offs. The LAPAN-A3 mission employed a full-unit Mu-metal shield for its RWA, achieving measurable attenuation but nearly doubling the RWA mass [22]. Similarly, NASA's Cassini spacecraft relied on extensive Mu-metal shielding to protect its magnetometer payload, achieving excellent suppression at the expense of substantial mass and integration penalties [25][26]. These experiences motivated subsequent designs to adopt partial or localized shielding strategies targeting dominant emission regions.

To reconcile competing requirements for attenuation, saturation resistance, and mass efficiency, recent studies have explored hybrid and multilayer shielding concepts. Approaches combining structural steels with inner high-permeability liners have demonstrated improved performance under strong magnetic excitation with reduced mass penalties [27]-[32]. Hybrid active–passive configurations and multilayer magnetic–conductive structures have also shown enhanced attenuation in static and low-frequency regimes [33] -[39], though their added complexity and power demands often limit applicability in small satellite platforms.

Despite extensive prior work, few studies have systematically quantified the combined influence of shielding material selection and thickness scaling within realistic small-satellite RWA geometries using a consistent numerical framework [40][41]. Most existing investigations rely on simplified geometries, isolated material comparisons, or non-mission-representative conditions. To address this gap, the present study applies three-dimensional finite element modeling to evaluate candidate shielding materials and thicknesses under identical excitation and boundary conditions in a reaction-wheel-representative configuration. The resulting analysis provides practical, design-oriented guidance for achieving magnetic cleanliness in small satellite platforms while respecting stringent mass and volume constraints.

2. FEM MODELLING AND SIMULATION APPROACH

Analytical solutions for magnetic shielding are

Table 1. Brushless DC motor specifications.

Specifications	Value
Nominal Voltage	48 V
Diameter	24 mm
Height	44 mm
Mass	98 g
No-load Speed	21600 min^{-1}
Housing Material	Alumninum, black anodized
Magnet Material	SmCo
Number of Pole Pairs	1
Hall Sensor	Digital
Phase	3
Back-EMF Constant (k_E)	2.22 mV/ min^{-1}
Magnet Remanence (B_r)[1]	1.15 Tesla
Peak Airgap Flux Density	1.1 Tesla

Source: Datasheet Brushless DC-Servomotors [42].
[1]The magnet remanence (B_r) was calculated from the back from the back-EMF constant (k_E) and the motor geometric parameters to establish the source strength for the FEM model

Table 2. Mesh sizing parameters.

Part	Mesh Size (mm)	Type	Element Shape	Cumulative Adaptive Elements (AMR)
Internal BLDC Motor	0.1–0.2	Fine	Tetrahedral	$1 \times 10^8 - 1.5 \times 10^7$
Magnetic Shielding Case	0.2–0.3	Fine	Tetrahedral	$5 \times 10^7 - 1.5 \times 10^6$
Internal Part RWA	0.5–1.0	Medium	Tetrahedral	$3.5 \times 10^7 - 4.5 \times 10^6$
Box Boundary	10	Coarse	Tetrahedral	$1.5 \times 10^6 - 3.5 \times 10^5$

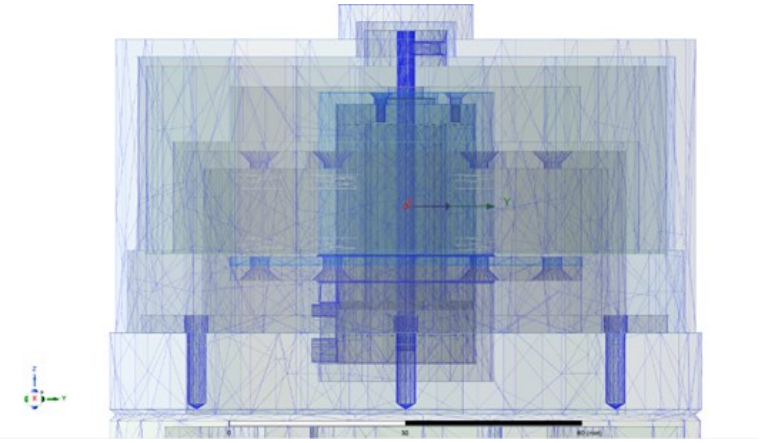

Figure 2. Finite element mesh configuration of the RWA motor and shielding assembly used in magnetostatic simulations, illustrating localized refinement in regions of high magnetic field gradients.

generally limited to idealized geometries such as infinitely long cylinders or perfectly closed shells, and typically assume linear magnetic material behavior. These assumptions are not representative of a realistic RWA, which involves finite-length enclosures, geometric discontinuities, and nonlinear ferromagnetic materials operating near saturation. As a result, analytical models can provide only qualitative or first-order estimates of shielding effectiveness. To overcome these limitations, this study employs three-dimensional finite element modeling, which enables direct numerical solution of Maxwell's equations under realistic geometry, boundary conditions, and nonlinear material properties. FEM is therefore well suited for evaluating magnetic shielding performance in satellite subsystems, where localized saturation, flux leakage, and geometry-dependent effects strongly influence overall attenuation.

In this study, the FEM simulations focus on mitigating the static magnetic field generated by the permanent magnet (PM) rotor, which constitutes the dominant and most challenging component of the RWA's magnetic emissions to shield due to its high amplitude and DC nature. While operational RWAs generate time-varying magnetic fields associated with stator currents and commutation, these effects are intentionally excluded, and the analysis is restricted to the magnetostatic field generated by the permanent-magnet rotor. This choice is physically motivated, as rotor-induced static fields in small-satellite reaction wheels are typically one to two orders of magnitude stronger than dynamic components and therefore govern saturation-limited shielding behavior. Focusing on the static field thus represents a conservative worst-case condition for passive magnetic shielding, ensuring that material nonlinearity and saturation effects are fully captured. While this assumption does not affect the relative ranking of materials or the thickness-dependent attenuation trends reported here, it limits the scope of the results to saturation-dominated performance and does not account for low-frequency magnetic noise arising from operational current variations.

2.1. Reaction Wheel Assembly Model

The modeled RWA reflects a configuration representative of small satellites under 200 kg and comprises several key components. The outer case serves as a structural enclosure, providing mechanical protection and electromagnetic

containment. A baseplate mechanically interfaces the RWA with the satellite bus. At the core of the assembly is a brushless DC motor consisting of a samarium–cobalt (SmCo) permanent magnet rotor and a laminated steel stator with copper windings. A flywheel is mounted to provide the angular momentum required for attitude control, while springs and dampers are incorporated to mitigate vibration transmission to the spacecraft structure.

Surrounding the motor is a conformal magnetic shielding enclosure designed to suppress stray magnetic emissions without interfering with mechanical integration or thermal management. Figure 1(a) shows the complete RWA assembly with the shielding enclosure, while Figure 1(b) illustrates a representative compact RWA design for small satellite applications. The permanent-magnet rotor represents the dominant static magnetic field source, whereas the stator windings constitute secondary, time-varying sources. Since internal suppression of these fields is impractical, external shielding is required to limit magnetic emissions at the spacecraft level. The brushless DC motor specifications used to parameterize the magnetic source are summarized in Table 1. The remanent flux density of the permanent magnet was derived from the back-EMF constant and motor geometry using standard electromagnetic motor relations, ensuring consistency between the FEM source definition and manufacturer-provided performance data.

2.2. FEM Formulation and Magnetic Field Modeling

Three-dimensional finite element simulations were conducted using ANSYS Maxwell in magnetostatic solver mode. Under this formulation, the magnetic field distribution is obtained by solving Maxwell's equations under time-invariant conditions, which is appropriate for evaluating the dominant static magnetic field produced by the permanent magnet rotor of the RWA. This approach enables accurate computation of magnetic flux density distributions in the presence of finite-length geometries and nonlinear ferromagnetic materials operating near saturation. The permanent magnet rotor was modeled using a fixed remanent magnetization vector, with its magnitude derived from the motor back-EMF constant and geometric parameters listed in Table 1. This ensures consistency between the FEM source definition and the electromagnetic characteristics of the brushless DC motor. All ferromagnetic components, including the shielding enclosure, were assigned nonlinear B–H curves obtained from manufacturer datasheets and validated literature sources to capture saturation effects accurately.

Within the FEM framework, magnetic field continuity and constitutive behavior are enforced implicitly at all material interfaces. In magnetostatic form, the governing relations can be expressed using the magnetic scalar potential formulation. The tangential magnetic field component is given by Equation (1);

$$H_t = -\nabla_t V_m \tag{1}$$

where V_m is the magnetic scalar potential and ∇_t denotes the tangential gradient operator. The corresponding magnetic flux density within a

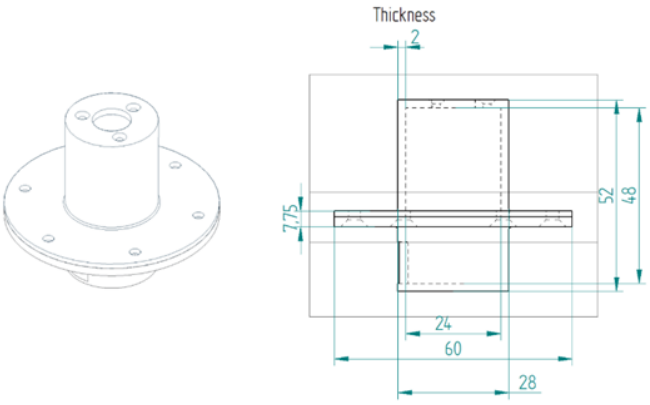

Figure 3. Engineering diagram of the cylindrical magnetic shielding showing isometric and cross-sectional dimensions.

Table 3. Electromagnetic and mechanical properties of candidate shielding materials.

	Aluminum 6061-T6	Mu-metal	Permalloy Fe-Ni	AISI 1008	AISI 1010
Relative Permeability (μ_r)	1	>80000	50000–100000	1000–4000	1500–3500
Saturation Flux Density (T)	Non-ferromagnetic	0.8	0.8–1.1	2.0–2.2	2.0–2.2
Coercivity (A/m)	0	2–5	2–10	8–120	8– 120
Resistivity ($\Omega \cdot$ m)	4.0×10^{-8}	5.5×10^{-7}	5.0×10^{-7}	1.6×10^{-7}	1.6×10^{-7}
Density (g/cm^3)	2.7	8.7	8.7	7.87	7.87
Tensile Strength (MPa)	310	550	500–600	340–420	350–430
Yield Strength (MPa)	276	280	200–300	180–240	180–260
Young's Modulus (GPa)	68.9	200	200	200–210	200–210
Cost	Low	Very High	High	Low	Low

Source: Material properties [45]-[51].

material is obtained through the constitutive relation (Equation (2));

$$B_t = \mu_0 \mu_r H_t \quad (2)$$

Where μ_0 permeability of free space and μ_r is the relative permeability, which varies with field intensity for nonlinear materials. These relations are not used as standalone analytical expressions but are implemented numerically within the FEM solver to enforce flux continuity, material nonlinearity, and interface behavior across the computational domain. This formulation enables accurate resolution of localized flux concentration and saturation effects that cannot be captured using analytical shielding models or scaling laws.

The resulting magnetic flux density magnitude was computed throughout the RWA and the surrounding space, providing the basis for evaluating magnetic shielding effectiveness (SE). In this study, passive magnetic shielding is treated as a flux-shunting mechanism, whereby high-permeability materials provide a low-reluctance path that redirects magnetic field lines away from the protected region. Accordingly, SE is quantified directly from the FEM-computed magnetic induction fields as the logarithmic ratio between the unshielded and shielded magnetic flux density magnitudes at specified observation locations (Equation (3));

$$SE = 20\, log_{10}\left(\frac{B_0}{B_1}\right) \quad (3)$$

Where B_0 and B_1 denote the magnetic flux density without and with the shielding enclosure, respectively. Because the simulations are performed under magnetostatic conditions and within linear air regions, this definition is equivalently expressed in terms of magnetic field intensity without loss of generality. The FEM-based SE evaluation inherently accounts for material nonlinearity, geometric effects, and saturation-induced degradation, which are critical factors in high-permeability shielding performance.

By restricting the analysis to the magnetostatic field generated by the permanent-magnet rotor, the simulations capture a conservative worst-case condition for passive magnetic shielding, under which high-permeability materials are most

susceptible to nonlinear saturation. This assumption is consistent with prior experimental and numerical studies indicating that rotor-induced static fields dominate the near-field magnetic environment of compact reaction wheel assemblies. Consequently, the reported SE values should be interpreted as upper-bound, saturation-limited performance metrics for passive shielding, rather than predictions of operational magnetic noise attenuation or AC shielding effectiveness.

2.3. Mesh Configuration and Simulation Procedure

The finite element mesh was generated using the tetrahedral meshing engine in ANSYS Maxwell. A hierarchical meshing strategy was adopted to balance numerical accuracy and computational efficiency. Fine mesh elements (0.1–0.3 mm) were applied to regions with high magnetic field gradients, including the rotor magnets, stator region, and magnetic shielding layers. Medium-resolution elements (0.5–1.0 mm) were assigned to internal RWA components, while coarser elements (up to 10 mm) were used in the surrounding air domain. The element counts reported in Table 2 do not correspond to a single global mesh. Instead, they represent the cumulative number of elements generated across successive adaptive mesh refinement (AMR) iterations. Localized refinement was automatically applied in regions exhibiting high magnetic field gradients, particularly within the permanent magnet rotor, air gap, and thin shielding layers. The final converged mesh contained substantially fewer active elements than the cumulative total, ensuring computational tractability while preserving numerical accuracy.

The magnetostatic solver employed second-order interpolation with a relative residual convergence threshold of 10^{-5}, which ensures numerical accuracy for magnetostatic field solutions while maintaining reasonable computational efficiency [43][44]. AMR was enabled to dynamically increase mesh density in regions of high field gradient, thereby improving solution accuracy without unnecessarily refining the entire model. Convergence was typically reached within 10 iterations, indicating a well-posed problem and efficient solver setup [45].

A mesh-independence assessment was performed by comparing the shielding effectiveness at the 100-mm reference distance between the final AMR refinement steps. Convergence was defined as a variation in SE of less than 2% between successive refinements. Further reductions in characteristic element size below approximately 10% produced less than 1.5% change in magnetic flux density at 100 mm, confirming that additional refinement would not materially improve accuracy. To further assess numerical robustness, a limited sensitivity study was conducted. Key model parameters (relative permeability, shield thickness,

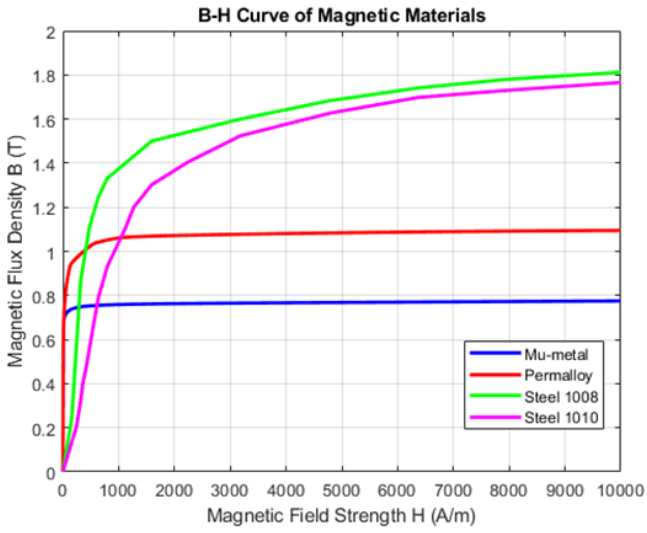

Figure 4. B-H curves of candidate shielding materials implemented in FEM simulations [46]. B–H curves imported into the FEM solver are taken directly from digitized manufacturer and literature data, processed only for smoothing and interpolation, and implemented without rescaling or artificial enhancement.

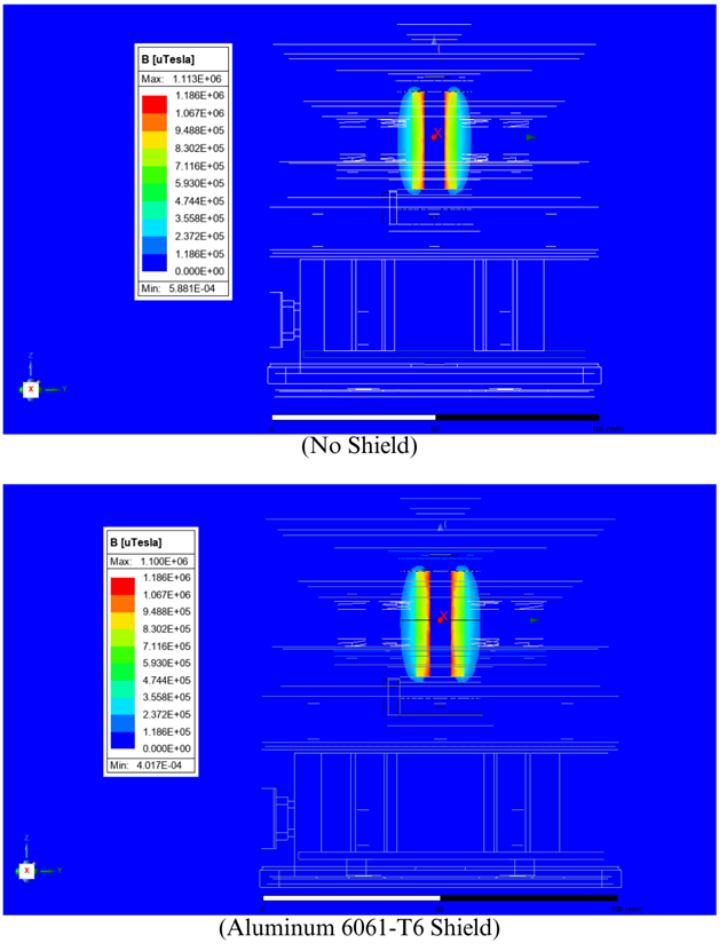

Figure 5. Magnetic flux density magnitude (B) distribution in the reaction wheel assembly (RWA) under magnetostatic excitation from the permanent-magnet rotor: (top) unshielded configuration, and (bottom) aluminum 6061-T6 casing used as a non-magnetic baseline.

and magnet remanence) were perturbed by ±5%. The resulting variations in shielding effectiveness remained below 3% across all configurations, indicating that the FEM predictions are relatively insensitive to moderate modeling uncertainties. A full probabilistic uncertainty quantification is beyond the scope of this work and will be addressed in future studies. Magnetic flux density B(d) was then sampled along three orthogonal axes from 0 to 150 mm in 1-mm increments. The 100-mm position is retained as the primary reference distance for reporting SE results, while additional distances are used to illustrate spatial decay trends. An example of the final mesh configuration is shown in Figure 2.

3. MATERIALS AND CONFIGURATIONS

The shielding strategy in this study focuses on the BLDC motor, which represents the dominant magnetic emission source within the RWA. A cylindrical shield was designed to enclose the motor, providing both magnetic attenuation and structural support. The geometry was constrained by the motor dimensions (24 mm diameter, 44 mm height) and an integration envelope not exceeding 60 mm at the flange. Single-layer shields of 1, 2, and 3 mm thickness were modeled and evaluated (Figure 3), reflecting manufacturable thicknesses compatible with small-satellite mass and volume constraints.

Four candidate materials were selected for evaluation: Mu-metal, Fe–Ni Permalloy (80% Ni composition), AISI 1008 steel, and AISI 1010 steel. Aluminum 6061-T6 was included as a non-magnetic baseline. The magnetic response of each material was defined using nonlinear B–H curves so that permeability roll-off and saturation effects were captured accurately in ANSYS Maxwell (Table 3).

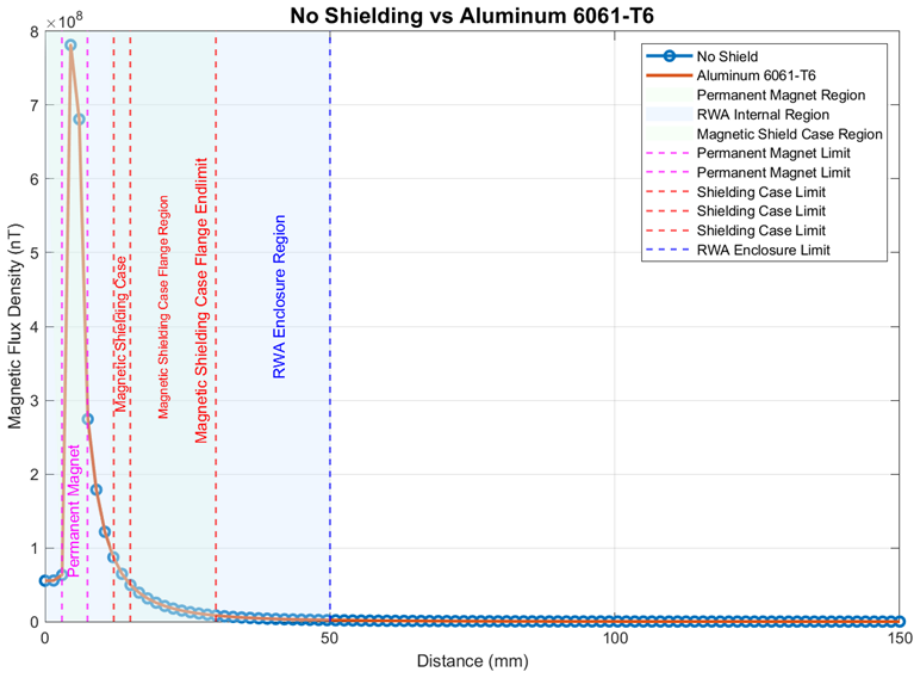

Figure 6. Magnetic flux density magnitude **(B)** as a function of radial distance from the motor central axis under magnetostatic excitation from the permanent-magnet rotor, comparing the unshielded configuration and an aluminum 6061-T6 casing used as a non-magnetic baseline.

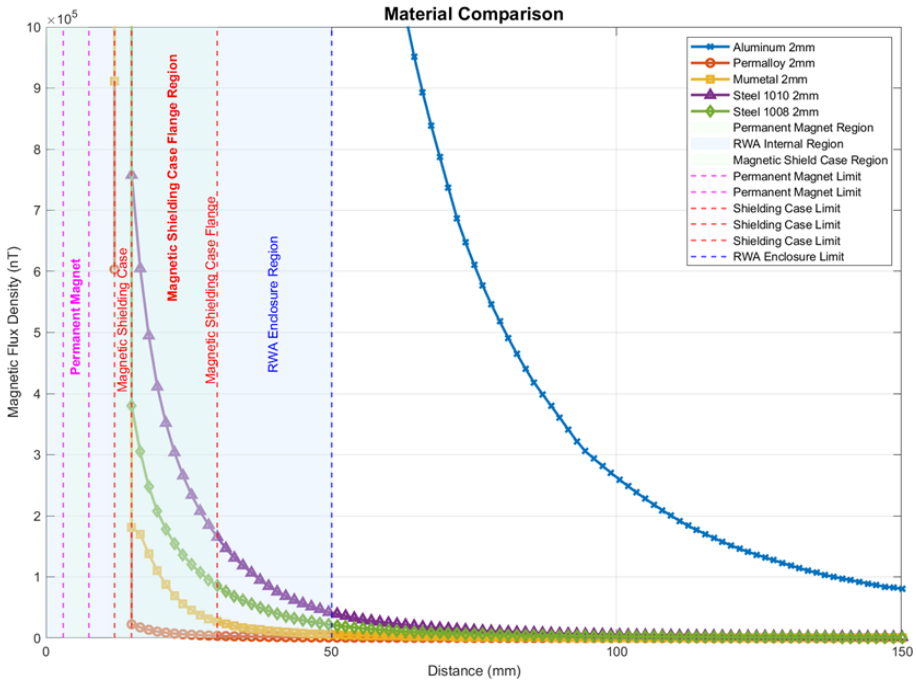

Figure 7. Magnetic flux density magnitude (B) profiles generated by the permanent-magnet rotor as a function of radial distance, comparing different shielding materials at a fixed thickness of 2 mm.

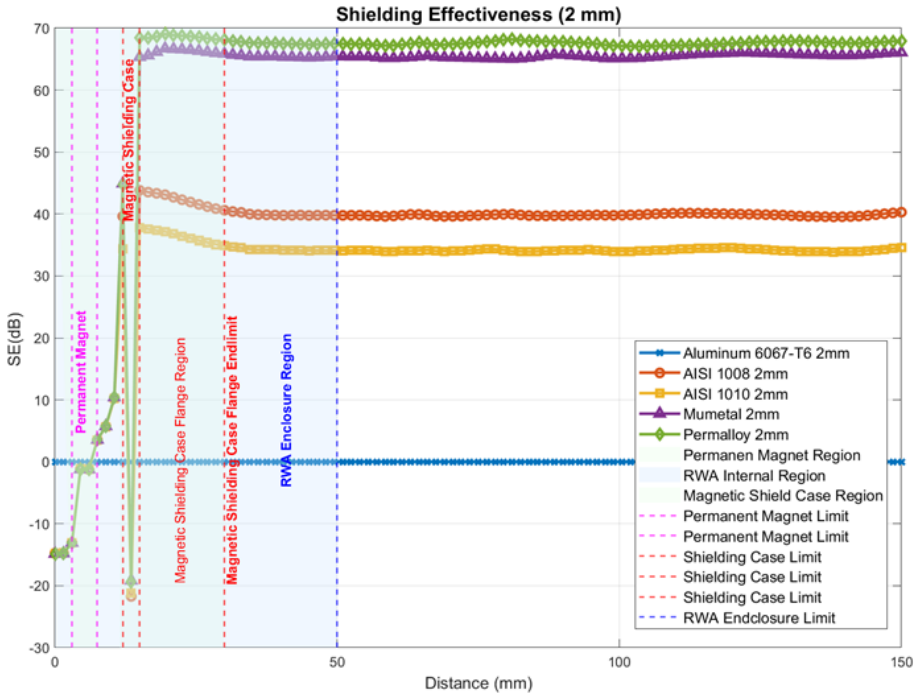

Figure 8. Magnetostatic shielding effectiveness (SE) versus radial distance for different 2 mm shielding materials under permanent-magnet rotor excitation.

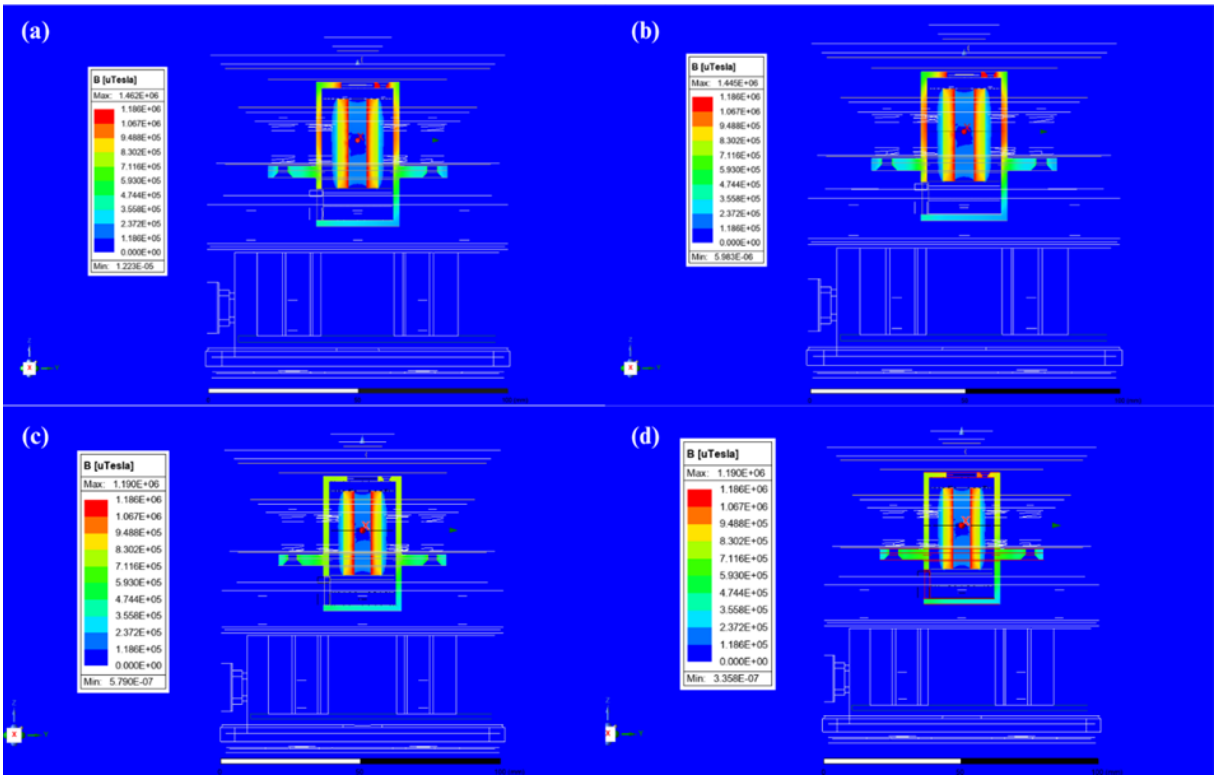

Figure 9. Magnetic flux density distributions for 2 mm shielding: (a) AISI 1008, (b) AISI 1010, (c) Mu-metal, (d) permalloy.

For each alloy, the B–H data were obtained from manufacturer datasheets and, where necessary, supplemented with curves reported in peer-reviewed literature for the same material grade. The curves were digitized and smoothed using spline interpolation to remove sampling noise while preserving the knee region and the high-field slope. No scaling or empirical tuning was applied. For magnetic fields exceeding the highest tabulated value, the curves were extrapolated using the saturated slope reported in the datasheets to ensure numerical stability without artificially increasing the effective permeability.

High-permeability alloys (Mu-metal and Permalloy) offer excellent shielding at low flux densities due to their large μ_r values and low coercivity, but they are mechanically fragile, dense, and costly. Low-carbon steels (AISI 1008/1010) provide moderate permeability with higher saturation thresholds (2 T) and strong mechanical robustness, making them attractive for hybrid or mass-sensitive satellite designs. Aluminum 6061-T6 was included solely as a non-magnetic structural baseline to quantify the absence of passive magnetic shielding. Figure 4 displays the B–H curves used in the simulations, illustrating the nonlinear magnetic response of the candidate materials under varying field intensities [46].

4. RESULT AND DISCUSSION

This section presents and interprets the finite element analysis results of magnetic shielding applied to a brushless DC motor in a RWA. The discussion integrates spatial field distributions, quantitative shielding effectiveness, and material geometry trade-offs, with direct implications for small satellite magnetic cleanliness.

4.1. Baseline Magnetic Flux Behavior Without Shielding and with Aluminum Casing

Baseline simulations established the uncontrolled magnetic environment of the RWA. Figure 5 compares the flux density distribution without shielding and with an aluminum 6061-T6 enclosure. Figure 5 also display the simulation results, showing that for both the unshielded and aluminum -shielded cases, the magnetic field emanates from and encircles the motor assembly. The strongest field intensity (indicated by red regions) is concentrated on the motor housing surface itself, weakening progressively (transitioning to yellow, green, and blue) with increasing radial distance. As expected, the two cases are nearly indistinguishable due to aluminum's relative permeability of $\mu_r \approx 1.000022$).

The peak magnetic flux density on the inner surface of the motor housing is approximately 7.8×10^7 nT, dominated by the permanent magnet in the BLDC rotor. The field decays with radial distance, reaching 1.2×10^6 nT at 50 mm, 2.6×10^5 nT at 100 mm, and 8.27×10^4 nT at 150 mm (Figure 6). These results establish the uncontrolled dipole field distribution for subsequent shielding comparisons. To quantify performance, SE was evaluated relative to the unshielded case. For aluminum, SE remains within 0 dB across all radial distances, confirming negligible attenuation. By contrast, ECSS-E-ST-20-07C stipulates a magnetic cleanliness limit of ≤200 nT at 1 m for spacecraft hosting magnetometers or precision attitude sensors [25]. To translate this requirement to the 100 mm standoff distance relevant for small satellite integration, the dipolar nature of the field must be considered. Assuming a dipolar inverse-cube decay, this corresponds to an equivalent threshold of 200 μT at 100 mm. This calculated threshold of 200 μT at 100 mm provides a system-level goal for magnetic cleanliness. However, for the protection of ultra-sensitive payloads, a more stringent, commonly adopted goal is to achieve ≤1 μT) at 100 mm. Our unshielded field of 260 μT at 100 mm exceeds the ECSS-derived limit by approximately 30% and the stricter μT goal by a factor of 260.

From an engineering perspective, the baseline simulations confirm that unshielded or aluminum-encased RWAs generate magnetic contamination levels far above acceptable thresholds. This demonstrates that structural enclosures such as aluminum, despite their mechanical utility, contribute no meaningful shielding effect. As a result, aluminum casings must be supplemented with high-permeability or ferromagnetic materials whenever magnetic cleanliness is a design requirement. This establishes the reference condition against which all subsequent shielding analyses must be evaluated: namely, that an SE improvement of more than 48 dB at 100 mm is

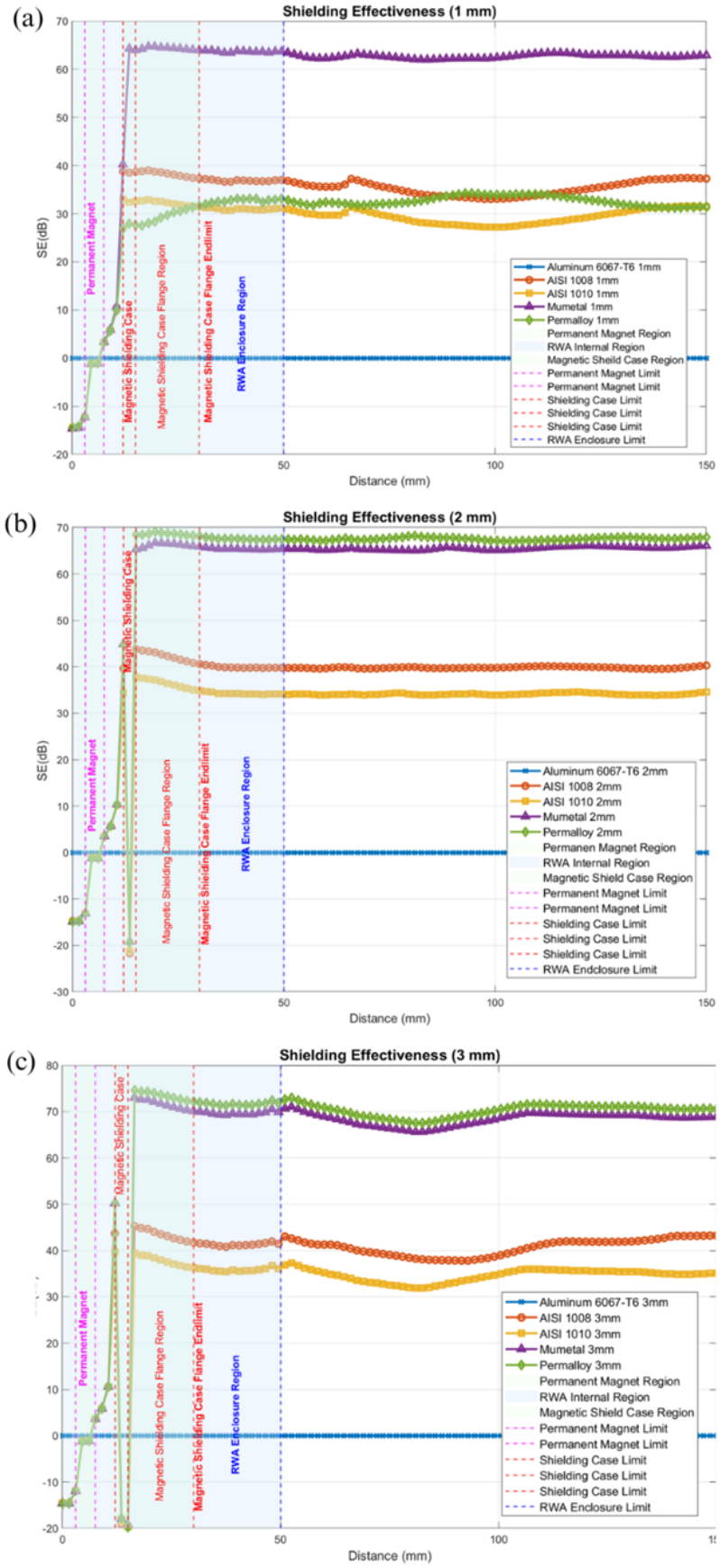

Figure 10. Shielding effectiveness (SE) versus radial distance for all materials at varying thicknesses: (a) 1 mm, (b) 2 mm, (c) 3 mm.

required to reduce the field from 260 µT to below 1 µT and meet stringent standards for sensitive payloads.

4.2. Effect of Shielding Material on Magnetic Attenuation

The influence of material choice on magnetic attenuation was evaluated using a uniform 2 mm shield thickness across all candidates. Figure 7 presents the radial flux density decay, while Figure 8 plots the corresponding shielding effectiveness.

By contrast, high-permeability alloys exhibit a dramatic improvement. At 150 mm, Mu-metal reduces the external field to 41 nT and permalloy 80 to 33.2 nT, corresponding to SE values of 66.1 and 67.9 dB, respectively. Both fall well below ESA and NASA field thresholds in 1 µT threshold, demonstrating their suitability for high-precision missions requiring sub-nT magnetometer stability. However, both alloys approach saturation near the motor casing, where flux density inside the shield walls exceeds 1100–1200 µT. Low-carbon steels provided intermediate performance. AISI 1008 and 1010 reduced the 150 mm field to 800 and 1540 nT, with SE values of 40.3 and 34.6 dB, respectively. These values are sufficient to meet the ECSS-E-ST-20-07C requirement (200 nT at 1 m) but exceed the stricter 1 µT at 100 mm limit often used for ultra-sensitive instruments. Their performance may be acceptable for less sensitive subsystems such as star trackers or sun sensors, especially if located further from the RWA. The steels' advantage lies in their higher saturation thresholds (2.0 T), enabling them to sustain higher near-field flux before performance degradation.

Figure 9 illustrates the spatial field distributions for all materials. Mu-metal and permalloy show tight confinement of flux lines within the enclosure, while steels exhibit visible leakage beyond the shield boundary. Aluminum, as expected, shows virtually no redirection of flux. The results further demonstrate that only high-permeability alloys such as Mu-metal and Permalloy are capable of reducing residual fields to the sub-micro-Tesla range required for the most stringent payload environments, though their use inevitably imposes significant penalties in both mass and cost. By contrast, low-carbon steels provide a more practical

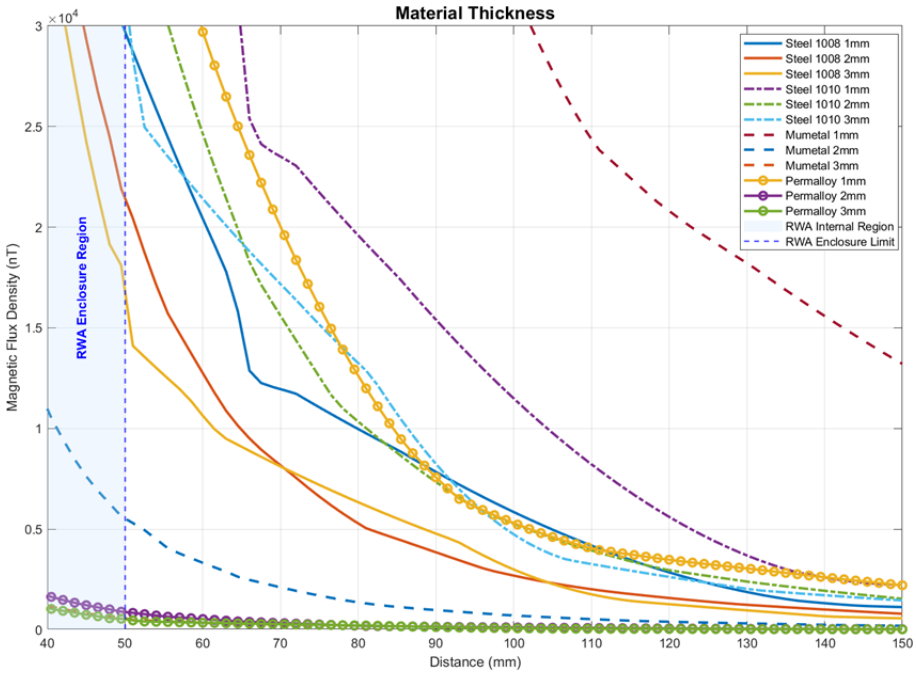

Figure 11. Line graphs of magnetic flux density (B) versus radial distance for all materials and thicknesses (1 mm, 2 mm, 3 mm), with aluminum included as the no-shield baseline. Profiles span the RWA regions, including the permanent magnet, stator, housing, shielding walls, and the external environment. Complementary to the SE trends in **Figure 10**, these results highlight that high-permeability alloys confine flux within the shielded walls more effectively, while steels rely more on increased thickness to achieve comparable attenuation.

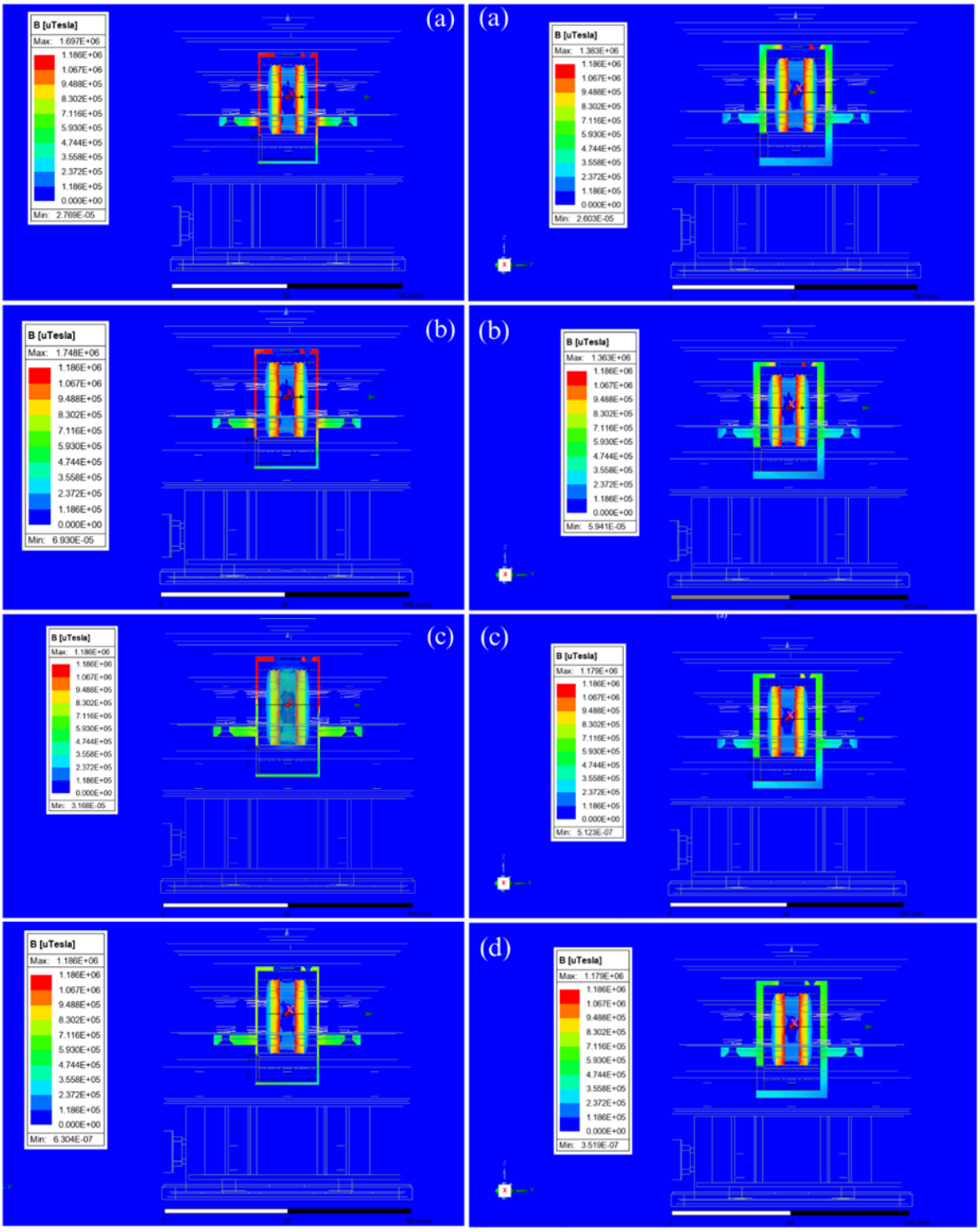

Figure 12. Two-dimensional magnetic flux density (B) maps for 1 mm (left) and 3 mm (right) thicknesses across all materials: (a) AISI 1008, (b) AISI 1010, (c) permalloy, and (d) Mu-metal. The maps illustrate the spatial role of the shielding walls as flux-confining regions: thicker steel walls reduce leakage more effectively, while Mu-metal and Permalloy show minimal change beyond 2 mm due to early flux confinement. The RWA regions (permanent magnet, stator, housing, shielding walls, and external environment) are annotated, with aluminum showing negligible redirection of flux. Cross-referenced with **Figures 11** and **12**, these visualizations reinforce the combined effects of material permeability and wall thickness.

Table 4. Shielding performance and mass comparison at 100 mm standoff distance.

Material	Thickness (mm)	SE (dB)	Approx. Mass (g)	SE / Mass (dB/kg)
AISI 1008	1	33	191	172.77
	2	39	226	172.57
	3	40	262	152.67
AISI 1010	1	27	191	141.36
	2	34	226	150.44
	3	35	262	133.59
Mu-metal	1	64	216	287.04
	2	65	250	260.00
	3	69	290	237.93
Permalloy 80	1	34	216	157.41
	2	67	250	268.00
	3	71	290	244.83

Note: Shield mass calculated for a cylinder of height 44 mm, inner diameter 24 mm

compromise, offering mechanical robustness and lower cost, but their limited attenuation performance means they struggle to satisfy ECSS magnetic cleanliness limits when sensitive instruments are located within 100 mm of the RWA. Aluminum, in turn, cannot be regarded as a shielding solution at all; its role remains purely structural, with negligible contribution to magnetic attenuation.

4.3. Effect of Shield Thickness on Attenuation

The impact of wall thickness was assessed for all candidate materials at 1, 2, and 3 mm (Figures 10–12). Results confirm that thickness exerts a significant yet non-linear influence on shielding performance, with behavior strongly governed by material permeability and saturation properties. For Mu-metal and Permalloy, even the thinnest configuration (1 mm) already achieves approximately 35 dB SE at 100 mm. Increasing the thickness to 2 mm enhances SE to roughly 55 dB, but further gains diminish due to early saturation near 0.8 T. At 3 mm, performance plateaus with less than 5 dB improvement relative to the 2 mm case, demonstrating that ultra-high-permeability alloys provide efficient shielding at minimal thickness but offer little benefit from additional mass. This behavior makes them particularly well-suited for CubeSat missions where tight mass budgets demand minimal shielding layers.

By contrast, low-carbon steels (AISI 1008 and 1010) exhibit more gradual scaling. At 1 mm, SE is limited to 10–15 dB at 100 mm, which is sufficient to meet the ECSS limit but is insufficient for the stricter 1 μT requirement at 100 mm. Increasing the thickness to 2 mm markedly improves attenuation, achieving 30–35 dB at 100 mm and 40 dB at 150 mm. At 3 mm, the steels reach 45–55 dB at 150 mm, approaching the performance of 2 mm Mu-metal. This progression reflects their higher saturation flux density (2.0–2.2 T), which allows steels to continue benefiting from added thickness without saturation losses.

Flux density distributions reinforce these trends. Figure 11 shows that for Mu-metal and Permalloy, the external flux stabilizes beyond 2 mm, while localized saturation emerges within the shield walls. For steels, the 3 mm enclosures confine flux more effectively, reducing external leakage by nearly 40% relative to the 1 mm case. Figure 12 visualizes the thickness effect, i.e., at 3 mm, steel enclosures confine flux more effectively within the shielding walls and noticeably reduce leakage into the external environment, whereas Mu-metal and permalloy show minimal improvement beyond 2 mm because most flux is already redirected at thinner sections. These observations suggest clear design strategies. For mass-constrained satellites, thin (1–2 mm) high-permeability alloy liners offer the best performance-to-mass trade-off, giving

strong attenuation with minimal added mass. Conversely, for missions where cost and mechanical robustness are primary concerns, 3 mm low-carbon steel shields deliver useful attenuation and superior saturation headroom, although they may not always meet magnetometer-class cleanliness requirements on their own. A practical compromise is a hybrid architecture in which a thin inner high-permeability liner is backed by a thicker steel shell; such a layered design can combine the near-source suppression of Mu-metal/permalloy with the saturation resistance and structural benefits of steel.

4.4. Mass and Performance Trade-off Analysis

Shielding performance must be assessed alongside mass, which is a critical constraint for small satellite platforms. The mass of each cylindrical enclosure was calculated from the material density (Table 3) and geometric volume (Figure 3). The resulting shielding effectiveness (SE) at 100 mm and corresponding mass values are summarized in Table 4.

Table 4 highlights a key trade-off: although all materials achieve attenuation sufficient to meet baseline cleanliness requirements, their mass efficiency differs substantially. In this study, mass efficiency is quantified using the ratio SE/m (dB/kg). This metric is adopted because spacecraft mass budgets penalize added mass independently of shield geometry, whereas thickness-based metrics (such as dB/mm) do not account for density differences between materials. For example, Mu-metal and low-carbon steel may provide similar SE at the same thickness, but their mass contributions differ significantly. Normalizing by mass therefore enables a fair comparison across materials and thicknesses on the basis of system-level mass impact.

The figure of merit SE per unit mass (dB/kg) shows that thinner shields (1 mm) consistently deliver the highest performance-to-mass ratio across all materials. This trend is particularly relevant for CubeSats and nanosatellites, where every gram is critical. Notably, 1 mm low-carbon steels achieve mass efficiencies comparable to high-permeability alloys, while also offering mechanical robustness and lower cost. Conversely, while thicker shields improve attenuation, they yield diminishing returns in SE per kilogram. These findings confirm that the optimal design for mass-constrained missions is a thin, high-performance shield, whereas thicker enclosures may only be justified when robustness or saturation tolerance is prioritized over efficiency. Beyond shielding performance and mass, practical spacecraft design also requires consideration of manufacturability, availability of space-qualified materials, long-term magnetic stability, thermal compatibility, and integration complexity. A full lifecycle assessment of these factors is beyond the scope of the present study; however, they should be addressed during subsequent design iterations and hardware prototyping, complementing the performance-oriented insights developed here.

4.5. Validation and Benchmarking of FEM Results

To validate the reliability of the FEM-predicted shielding effectiveness (SE), the simulation results were quantitatively compared with analytical predictions and literature-reported experimental and simulation data (Table 5). According to the classical SE scaling law (Equation (3)), the magnetic attenuation increases with both material permeability and thickness; however, the improvement saturates once the material approaches magnetic flux density saturation. This nonlinear trend was clearly reflected in the FEM outcomes, particularly for high-permeability materials such as Mu-metal and Permalloy 80, which exhibited diminishing SE gains beyond approximately 2 mm thickness. For engineering design, shielding effectiveness is often approximated using classical scaling laws relating SE to material permeability, shield thickness t, and characteristic enclosure dimension D.

$$SE \propto \frac{\mu_r t}{D} \tag{3}$$

As shown in **Table 5**, the FEM-predicted SE values show strong agreement with benchmark studies. For example, the present 2 mm Mu-metal model achieved 65 dB under DC excitation, closely matching the 64 dB experimentally reported by Nicolai et al. [18], with only a –1.5% deviation. Similarly, the 1 mm permalloy 80 simulation yielded 34 dB, which falls within 10% of the 38 dB measured experimentally by Grabchikov et al. [28].

Table 5. Comparison between FEM-predicted shielding effectiveness (SE) and literature-reported results for similar materials and configurations.

Study	Material	Thickness (mm)	Frequency	Method	SE (dB)	Deviation (%)
This work	Mu-metal	2	DC (Magnetostatic)	FEM (ANSYS)	65	
	Permalloy 80	1	DC (Magnetostatic)	FEM (ANSYS)	34	
	AISI 1008	3	DC (Magnetostatic)	FEM (ANSYS)	40	
	AISI 1010	3	DC (Magnetostatic)	FEM (ANSYS)	35	
Nicolai et al [15]	Mu-metal	2	0–100 Hz	Experiment	64	-1.5%
Grabchikov et al. [19]	Permalloy 80	1	DC (Magnetostatic)	Experiment	38	10%
Shen et al. [36]	AISI 1008	3	< 2 KHz	Simulation (COMSOL) & Experiment	34	-15%
S. He, & J. Zheng [35]	AISI 1010	3	DC (Magnetostatic)	FEM (ANSYS)	36	-2.8%

For ferromagnetic steels, the 3 mm AISI 1008 plate reached 40 dB, consistent with the 34 dB obtained by Shen et al. [24] using COMSOL and experimental validation (–15% deviation). Likewise, the predicted 35 dB for 3 mm AISI 1010 aligns closely (–2.8%) with the 36 dB reported by He and Zheng [23].

Overall, the deviations between FEM predictions and literature values remain within 1–15%, which is consistent with reported accuracy for quasi-static magnetic FEM analysis. This agreement provides supporting evidence that the implemented modeling approach and material characterization are reasonable. However, no dedicated experimental validation was performed for the specific RWA shielding configuration considered here. Consequently, the present results should be interpreted as validated only at the model-level. Future work will therefore include hardware prototyping and experimental measurements under representative magnetic environments, together with extension of the framework to dynamic and frequency-dependent shielding effects.

4.6. Design Guidance and Engineering Implications for Spacecraft RWA

The FEM results demonstrate a quantifiable trade-off between shielding performance, mass, and cost, emphasizing that no single material universally optimizes all parameters. Instead, material selection must be tailored to mission constraints particularly payload magnetic sensitivity, allowable mass, and mechanical robustness. The engineering implications are summarized in Table 6.

n high-sensitivity missions, thin high-permeability alloys (1–2 mm) provide the strongest attenuation (>65 dB at 100 mm, residual fields <150 nT) and the highest SE-to-mass ratio (>700 dB/kg). These are ideal for magnetometer-bearing nanosatellites operating under tight mass budgets. For low-cost or mechanically demanding missions, low-carbon steels (AISI 1008/1010) remain practical, achieving up to 55 dB at 3 mm with inherent structural function and tolerance to higher flux densities. Finally, hybrid architectures a thin Mu-metal or Permalloy liner coupled with a steel shell offer a performance compromise, maintaining

Table 6. Recommended shielding materials and configurations for small-satellite Reaction Wheel Assemblies (RWAs), summarizing typical performance, efficiency, and suitable mission applications.

Material / Configuration	Typical SE @100 mm (dB)	Mass Efficiency (dB/kg)	Saturation Limit (T)	Recommended Application	Key Advantages / Limitations
Mu-metal / Permalloy (1–2 mm)	60–70	>700	0.8	CubeSats, nanosats with fluxgate or magnetometer payloads (<100 mm proximity)	Exceptional attenuation and magnetic cleanliness; limited by low saturation, fragility, and cost.
AISI 1008 / 1010 Steel (2–3 mm)	34–55	150–175	2.2	Small satellites with moderate sensitivity payloads (e.g., star trackers, coarse sensors)	Mechanically robust, low-cost, dual-use as structure; moderate attenuation.
Hybrid Shield (1 mm Mu-metal + 2 mm Steel)	60–65	Approx. 500	2.0	Microsatellites or missions requiring both structural durability and magnetic cleanliness	Balanced performance: high attenuation, high saturation tolerance, manufacturable configuration.

sub-μT external fields while ensuring mechanical integrity and manufacturability. Overall, the results establish a design matrix linking magnetic cleanliness requirements with material and thickness selection. This matrix enables spacecraft engineers to make evidence-based decisions balancing performance, cost, and robustness in next -generation small satellite reaction wheel assemblies.

5. CONCLUSIONS

This study employed three-dimensional finite element modelling to quantitatively assess magnetic shielding strategies for small-satellite reaction wheel assemblies (RWAs) under a unified and design-oriented framework. The results demonstrate that unshielded and aluminum-cased RWAs generate residual magnetic fields on the order of 260 μT at 100 mm, exceeding typical magnetic cleanliness requirements for precision payloads by more than five orders of magnitude. Aluminum structural materials were shown to provide negligible attenuation (<1 dB), confirming that dedicated ferromagnetic shielding is essential for magnetically sensitive missions. High-permeability alloys (Mu-metal and Permalloy 80) exhibited the highest shielding effectiveness, achieving more than 65 dB attenuation with a 2 mm thickness and reducing external fields to below 150 nT at 100 mm. However, performance gains diminished beyond this thickness due to material saturation limits. Low-carbon steels (AISI 1008/1010) provided moderate attenuation (34–40 dB at 2 mm) but offered higher saturation flux density, superior mechanical robustness, and significantly lower cost. Mass-efficiency analysis indicated that thin high-permeability alloys deliver the greatest attenuation per unit mass, favoring CubeSat-class platforms, while low-carbon steels remain attractive for larger small satellites emphasizing structural integration and manufacturability. Based on these complementary characteristics, hybrid shielding architectures combining low-carbon steel and high-permeability liners are recommended, with simulations predicting residual fields below 100 nT at 100 mm. Overall, the study contributes an RWA-specific FEM-based assessment methodology that captures nonlinear saturation, thickness scaling, and mass trade-offs beyond simplified analytical models. Experimental validation and inclusion of time-varying effects remain important directions for future work.

AUTHOR INFORMATION

Corresponding Author

Hogan Eighfansyah Susilo — Research Centre for Satellite Technology, National Research and Innovation Agency (BRIN), Bogor-16310 (Indonesia);
orcid.org/0000-0002-8176-7101
Email: hoga001@brin.go.id

Authors

Poki Agung Budiantoro — Research Centre for Satellite Technology, National Research and Innovation Agency (BRIN), Bogor-16310 (Indonesia);
orcid.org/0009-0001-6534-9655

Ery Fitrianingsih — Research Centre for Satellite Technology, National Research and Innovation Agency (BRIN), Bogor-16310 (Indonesia);
orcid.org/0009-0005-8039-4605

Hasan Mayditia — Research Centre for Satellite Technology, National Research and Innovation Agency (BRIN), Bogor-16310 (Indonesia);
orcid.org/0009-0001-3884-8467

Eriko Nasemudin Nasser — Research Centre for Satellite Technology, National Research and Innovation Agency (BRIN), Bogor-16310 (Indonesia);
orcid.org/0009-0006-0836-3860

Adi Farmasiantoro — Research Centre for Satellite Technology, National Research and Innovation Agency (BRIN), Bogor-16310 (Indonesia);
orcid.org/0009-0009-9891-898X

Ahmad Fauzi — Research Centre for Satellite Technology, National Research and Innovation Agency (BRIN), Bogor-16310 (Indonesia);
orcid.org/0000-0002-1306-8448

Widodo Slamet — Research Centre for Satellite Technology, National Research and Innovation Agency (BRIN), Bogor-16310 (Indonesia);
orcid.org/0009-0003-1467-5017

Andi Mukhtar Tahir — Research Centre for Satellite Technology, National Research and Innovation Agency (BRIN), Bogor-16310 (Indonesia);
orcid.org/0009-0002-5630-5682
Nindhita Pratiwi — Atmospheric and Planetary Science Department, Institut Teknologi Sumatera, Lampung Selatan-35365 (Indonesia);
orcid.org/0009-0008-9631-216X

Author Contributions

Conceptualization, H. E. S., P. A. B. and H. M.; Methodology, H. E. S. and P. A. B.; Software, Visualization, and Writing – Original Draft Preparation, H. E. S.; Validation, E. F., W. S. and H. M.; Formal Analysis, H. E. S. and E. F.; Investigation, E. N. N. and A. F.(1).; Resources, P. A. B. and H. M.; Data Curation, H. E. S., A. F.(2). and A. M.; Writing – Review & Editing, E. F. and N. P.; Supervision, P. A. B. and E. F.; Project Administration, E. N.; Funding Acquisition, P. A. B.

Conflicts of Interest

The authors declare that they have no known competing financial interests or personal relationships that could have appeared to influence the work reported in this paper.

ACKNOWLEDGEMENT

The authors would like to thank the Research Center for Satellite Technology, National Research and Innovation Agency (BRIN), Indonesia, for their support and for providing the funding and required facilities to conduct the research [CFC 04.53].

DECLARATION OF GENERATIVE AI

Not applicable.

REFERENCES

[1] A. Elshaal, M. Okasha, E. Sulaeman, A. H. Jallad, W. Faris Aizat, and A. B. Alzubaidi. (2024). "Structural Analysis of AlAinSat-1 CubeSat". *The Egyptian Journal of Remote Sensing and Space Sciences.* **27** (3): 532-546. 10.1016/j.ejrs.2024.06.006.

[2] A. Sanny, P. Gatkine, L. García Varela, H. García Vázquez, F. G. Témich, L. F. Rodríguez Ramos, N. Jovanovic, H. P. Stahl, and J. W. Arenberg. (2025). "Towards space-qualification of astrophotonic devices in the optical/IR". the UV/Optical/IR Space Telescopes and Instruments: Innovative Technologies and Concepts XII.

[3] P. S. Narvaez. (2018). In: "Handbook of Aerospace Electromagnetic Compatibility". Wiley. 621-672. 10.1002/9781119082880.ch12.

[4] R. H. Triharjanto, W. Hasbi, A. Widipaminto, M. Mukhayadi, and U. Renner. (2004). "LAPAN-TUBSAT: Micro-Satellite Platform for Surveillance and Remote Sensing". *Proceedings of the 4S Symposium: Small Satellites, Systems and Services (ESA SP-571)*. La Rochelle, France.

[5] S. Hardhienata, R. H. Triharjanto, and M. Mukhayadi. (2011). "LAPAN-A2: Indonesian Near-Equatorial Surveillance Satellite". *Proceedings of the 18th Asia-Pacific Regional Space Agency Forum (APRSAF)*. Singapore.

[6] W. Hasbi and Suhermanto. (2013). "Development of LAPAN-A3/IPB Satellite: An Experimental Remote Sensing Microsatellite". *Proceedings of the 34th Asian Conference on Remote Sensing (ACRS 2013)*.

[7] M. Mukhayadi, R. Madina, and U. Renner. (2014). "Attitude Control of Bias Momentum Micro-Satellite Using Magnetic and Gravity Gradient Torque". *Proceedings of the IEEE International Conference on Aerospace Electronics and Remote Sensing Technology (ICARES)*. 132-136. 10.1109/ICARES.2014.7024395

[8] M. A. Saifudin and M. Mukhayadi. (2015). "Attitude Determination and Control System (ADCS) of LAPAN-A2/ORARI Satellite". *Media Dirgantara.* 39-46.

[9] M. Mukhayadi. (2021). "Efficient and High Precision Momentum Bias Attitude Control for Small Satellites". Technische Universität Berlin.

[10] S. Utama, P. R. Hakim, and M. Mukhayadi. (2019). "Quarter Orbit Maneuver Using

Magnetorquer to Maintain Spacecraft Angular Momentum". **284** : 012046. 10.1088/1755-1315/284/1/012046

[11] X. Chen, S. Liu, T. Sheng, Y. Zhao, and W. Yao. (2019). "Satellite Layout Optimization Design Approach for Minimizing the Residual Magnetic Flux Density of Micro- and Nanosatellites". *Acta Astronautica.* **163** : 299-306. 10.1016/j.actaastro.2018.12.006.

[12] E. Carrubba, A. Junge, F. Marliani, and A. Monorchio. (2014). "Particle Swarm Optimization for Multiple Dipole Modeling of Space Equipment". *IEEE Transactions on Magnetics.* **50**. 10.1109/TMAG.2014.2334277.

[13] A. Giordani, G. M. Mongini, and E. Scione. (2024). "Magnetic Cleanliness Management in Small Satellites". *Proceedings of the International Symposium on Electromagnetic Compatibility (EMC Europe 2024)*. 98-103. 10.1109/EMCEurope59828.2024.10722399

[14] C. Jager. (2017). "Determination and Compensation of Magnetic Dipole Moment in Application for a Scientific Nanosatellite Mission". KTH Royal Institute of Technology.

[15] A. Lassakeur and C. Underwood. (2019). "Magnetic Cleanliness Program on CubeSats for Improved Attitude Stability". *Proceedings of the 9th International Conference on Recent Advances in Space Technologies (RAST)*. 123-129. 10.1109/RAST.2019.8767816

[16] T. Inamori, N. Sako, and S. Nakasuka. (2011). "Magnetic Dipole Moment Estimation and Compensation for an Accurate Attitude Control in Nano-Satellite Missions". *Acta Astronautica.* **68** : 2038-2046. 10.1016/j.actaastro.2010.10.022.

[17] A. Annenkova, N. Abdelrahman, D. Ivanov, D. Roldugin, and D. Pritykin. (2020). "CubeSat Magnetic Atlas and In-Orbit Compensation of Residual Magnetic Dipole". *Proceedings of the International Astronautical Congress (IAC 2020)*.

[18] A. Nicolai, S. Stoltz, O. Hillenmaier, J. Ludwig, C. Strauch, D. Grivon, L. Rossini, E. Onillon, T. Hellwig, and S. Scheiding. (2019). "Towards a Magnetically Clean Reaction Wheel with Active Magnetic Field Mitigation". *ESA Workshop on Aerospace Electromagnetic Compatibility*. 10.23919/AeroEMC.2019.8788947.

[19] D. A. Nicolai. (2019). "Magnetic Field Mitigation Strategies Towards a Magnetically Clean Reaction Wheel".

[20] S. Yang, X. Zhang, J. Gao, Y. Liu, J. Zhang, and X. Xi. (2022). "FEA Simulations for Low-Frequency Multi-Layer Magnetically Shielded Rooms". *AIP Advances.* **12** (8): 085325. 10.1063/5.0093443.

[21] X. Xu, W. Liu, Y. Huang, W. Li, and S. Che. (2023). "Magnetic Shielding Mechanism and Structure Design of Composites at Low Frequency: A Review". *Journal of Magnetism and Magnetic Materials.* **570** : 170509. 10.1016/j.jmmm.2023.170509.

[22] S. Utama, D. El Amin, M. A. Saifudin, M. F. Huzain, W. Roza, C. T. Judianto, and M. Mukhayadi. (2024). "Magnetic Shielding Implementation in the Small Satellite Reaction Wheel". *INCAS Bulletin.* **16** (1): 107-116. 10.13111/2066-8201.2024.16.1.11.

[23] S. He and J. Zheng. (2024). "Magnetic Shielding Design for the Carriage Structure of Superconducting EDS Transport System". *IEEE Transactions on Applied Superconductivity.* **34** (8): 1-4. 10.1109/TASC.2024.3420292.

[24] N. Shen, X. Zhang, Q. Liao, and M. Zhang. (2017). "Design and Experimental Analysis of Magnetic Shielding of Electronic-Magnetic Rail Gun Ammunition Fuse". *International Journal of Applied Electromagnetics and Mechanics.* **53** (2): 337-358. 10.3233/JAE-160060.

[25] P. Narvaez. (2004). In: "Cassini–Huygens Mission". Kluwer Academic Publishers. 385-394. 10.1007/978-1-4020-2774-1_5.

[26] M. G. Kivelson, X. Jia, K. A. Lee, C. A. Raymond, K. K. Khurana, M. O. Perley, and L. Wigglesworth. (2023). "The Europa Clipper Magnetometer". *Space Science Reviews.* **219** : 48. 10.1007/s11214-023-00989-5.

[27] K. Dang, P. Narvaez, J. Berman, K. Pham, and A. Curiel. (2020). "Magnetic Shielding Concepts for Reaction Wheel Assembly on

NASA Europa Clipper Spacecraft". *IEEE International Symposium on Electromagnetic Compatibility, Signal and Power Integrity (EMC+SIPI)*. 305-311. 10.1109/EMCSI38923.2020.9191616.

[28] S. S. Grabchikov, A. V. Trukhanov, S. V. Trukhanov, I. S. Kazakevich, A. A. Solobay, V. T. Erofeenko, N. A. Vasilenkov, O. S. Volkova, and A. Shakin. (2016). "Effectiveness of the Magnetostatic Shielding by the Cylindrical Shells". *Journal of Magnetism and Magnetic Materials.* **398** : 49-53. 10.1016/j.jmmm.2015.08.122.

[29] T. Liu, A. Schnabel, L. Li, Z. Sun, and J. Voigt. (2016). "Impact of Circular Apertures on Static Shielding Performances of Spherical Magnetic Shields". *IEEE Magnetics Letters.* **11** : 1-5. 10.1109/LMAG.2020.3042135.

[30] A. Mager. (1970). "Magnetic Shields". *IEEE Transactions on Magnetics.* **6** (1): 67-75. 10.1109/TMAG.1970.1066714.

[31] X. Yang, Z. Zhang, F. Ning, C. Jiao, and L. Chen. (2020). "Shielding Effectiveness Analysis of the Conducting Spherical Shell with a Circular Aperture against Low-Frequency Magnetic Fields". *IEEE Access.* **8** : 79844-79850. 10.1109/ACCESS.2020.2988709.

[32] E. Baum and J. Bork. (1991). "Systematic Design of Magnetic Shields". *Journal of Magnetism and Magnetic Materials.* **101** (1-3): 69-74. 10.1016/0304-8853(91)90682-Z.

[33] Y. Gao, X. Fang, D. Ma, B. Sun, K. Wang, S. Li, Y. Dou, and M. Zeng. (2024). "Analysis and Measurement of Magnetic Noise in a Multilayer Magnetic Shielding System Combined with Mu-Metal and Ferrite for Atomic Sensors". *Measurement.* **233** : 114745. 10.1016/j.measurement.2024.114745.

[34] Y. Liu, J. Yang, F. Cao, X. Zhang, and S. Zheng. (2024). "Enhancement of Magnetic Shielding Based on Low-Noise Materials, Magnetization Control, and Active Compensation: A Review". *Materials (Basel).* **17** (22). 10.3390/ma17225469.

[35] S. Firdosy, N. Ury, K. Dang, P. S. Narvaez, R. P. Dillon, and V. A. Ravi. (2023). "Additively Manufactured High-Permeability Fe-Ni Alloys and Novel Bi-Metallic Magnetic Shields". *Journal of Magnetism and Magnetic Materials.* 171049. 10.1016/j.jmmm.2023.171049.

[36] A. E. M. Mohamed, J. Zou, R. Sheridan, K. Bongs, and M. M. Attallah. (2020). "Magnetic Shielding Promotion via the Control of Magnetic Anisotropy and Thermal Post-Processing in Laser Powder Bed Fusion Processed NiFeMo-Based Soft Magnet". *Additive Manufacturing.* **32** : 101079. 10.1016/j.addma.2020.101079.

[37] Q. Meng, Z. Wang, Q. Lin, D. Ju, X. Liang, and D. Xian. (2024). "Theoretical Analysis of a Magnetic Shielding System Combining Active and Passive Modes". *Nanomaterials.* **14** (6): 538. 10.3390/nano14060538.

[38] S. Yu, J. Sun, H. Zhang, B. Han, and Z. Yang. (2025). "Analysis of Passive Shielding Performance Stability in Hybrid Magnetic Shielding Devices". *Applied Sciences.* **15** (24): 13173. 10.3390/app152413173.

[39] J. Victoria, A. Suarez, P. A. Martinez, A. Amaro, A. Alcarria, J. Torres, R. Herraiz, V. Solera, V. Martinez, and R. Garcia-Olcina. (2024). "Advanced Characterization of a Hybrid Shielding Solution for Reducing Electromagnetic Interferences at Board Level". *Electronics.* **13** (3): 598. 10.3390/electronics13030598.

[40] X. Xu, W. Liu, Z. Zhao, Y. Huang, and T. Zhu. (2024). "Efficient Magnetic Shielding by Designing Layered Composites with Nanocrystalline and Permalloy for Weak Magnetic Measurement". *Sensors and Actuators A: Physical.* **375** : 115538. 10.1016/j.sna.2024.115538.

[41] A. Getman. (2023). "Improving the Technology for Ensuring the Magnetic Cleanliness of Small Spacecraft". *Eastern-European Journal of Enterprise Technologies.* **123** (5). 10.15587/1729-4061.2023.282444.

[42] D. Cristina, U. Gheorghe, B. Gheorghe, and O. Radu. (2012). "Numerical simulation of the sensorless control for an electrical drive system with brushless DC servomotor". *the 2012 International Conference and*

Exposition on Electrical and Power Engineering.

[43] O. C. Zienkiewicz, R. L. Taylor, and J. Z. Zhu. (2013). "The Finite Element Method: Its Basis and Fundamentals". Elsevier. Oxford, United Kingdom.

[44] C. Hazard and S. Lohrengel. (2002). "A Singular Field Method for Maxwell's Equations: Numerical Aspects for 2D Magnetostatics". *SIAM Journal on Numerical Analysis.* **40** (3): 1021-1040. 10.1137/s0036142900375761.

[45] C. D. Munz, P. Ommes, and R. Schneider. (2000). "A three-dimensional finite-volume solver for the Maxwell equations with divergence cleaning on unstructured meshes". *Computer Physics Communications.* **130** (1-2): 83-117. 10.1016/s0010-4655(00)00045-x.

[46] E. M. Clements, R. Das, M.-H. Phan, L. Li, V. Keppens, D. Mandrus, M. Osofsky, and H. Srikanth. (2018). "Magnetic field dependence of nonlinear magnetic response and tricritical point in the monoaxial chiral helimagnet Cr1/3NbS2". *Physical Review B.* **97** (21). 10.1103/PhysRevB.97.214438.